nature physics

ARTICLES

PUBLISHED ONLINE: 3 AUGUST 2014 | DOI: 10.1038/NPHYS3040

Forces driving epithelial wound healing

Agustí Brugués[1†], Ester Anon[1,2†], Vito Conte[1†], Jim H. Veldhuis[3], Mukund Gupta[4], Julien Colombelli[5], José J. Muñoz[6], G. Wayne Brodland[3], Benoit Ladoux[2,4*] and Xavier Trepat[1,7,8*]

A fundamental feature of multicellular organisms is their ability to self-repair wounds through the movement of epithelial cells into the damaged area. This collective cellular movement is commonly attributed to a combination of cell crawling and 'purse-string' contraction of a supracellular actomyosin ring. Here we show by direct experimental measurement that these two mechanisms are insufficient to explain force patterns observed during wound closure. At early stages of the process, leading actin protrusions generate traction forces that point away from the wound, showing that wound closure is initially driven by cell crawling. At later stages, we observed unanticipated patterns of traction forces pointing towards the wound. Such patterns have strong force components that are both radial and tangential to the wound. We show that these force components arise from tensions transmitted by a heterogeneous actomyosin ring to the underlying substrate through focal adhesions. The structural and mechanical organization reported here provides cells with a mechanism to close the wound by cooperatively compressing the underlying substrate.

Wound healing is a central physiological process that involves a complex interplay between inflammation and tissue remodelling[1–3]. Impaired wound healing has a significant clinical impact in a variety of widespread diseases such as diabetes, chronic inflammatory disorders, vascular diseases and auto-immune diseases[2–4]. Moreover, there is a well-established association between aberrant wound healing and cancer progression[5].

A crucial step of the wound-healing response is the restoration of a continuous epithelial layer to recover tissue homeostasis, regain barrier integrity, and protect organisms from infection[4,6]. Epithelial repair is achieved through the collective movement of wound-bordering cells into the wound bed. To account for this collective movement, two main mechanisms are commonly invoked[1–3,6–11]. The first one is the assembly of a supracellular actomyosin ring at the wound margin, whose contraction drives the wound edges together like a purse-string[10,12–16]. The second mechanism is collective migration of marginal and submarginal cells led by lamellipodial and filopodial protrusions[17–21].

Extensive evidence supports the coexistence of a supracellular actomyosin ring and lamellipodial protrusions at the wound margin[8–11,22,23]. How these cytoskeletal structures drive wound closure remains incompletely understood, however, because the underlying physical forces have not been accessible to direct experimental observation. To provide the first maps of these physical forces, here we combined traction-force microscopy and laser ablation. We seeded a monolayer of Madin Darby canine kidney (MDCK) cells stably expressing LifeAct–GFP on top of a soft collagen-coated polyacrylamide gel containing fluorescent bead markers. Once the monolayer reached confluence and relatively high density, a cluster of ∼20 cells (∼5,000 μm^2) was ablated by recurrently targeting apical cell surfaces with a sub-nanosecond pulsed laser (Fig. 1a–c and Methods). Immediately after ablation, targeted cells lost a substantial amount of their F-actin content and surrounding cells retracted outwardly.

Following rapid tissue retraction, cells began to invade the wound area and to extrude ablated cells (Supplementary Movie 1). The onset of this wound-closure phase involved rapid protrusion of lamellipodia and filopodia towards the wound area (Fig. 1d). With a delay of ∼15 min, cell protrusion was followed by accumulation of actin and myosin at the wound edge (Fig. 1e,g–l). Formation of this supracellular actomyosin ring did not inhibit cell protrusions, which remained visible throughout closure (Fig. 1d–f). Both marginal and submarginal cells progressively acquired an elongated shape and constricted their front edge so as to create a rosette-like geometry by the end of wound closure (Fig. 1f). Throughout the process, cells remained tightly connected to their neighbours through adherens junctions and tight junctions (Supplementary Fig. 1a,b).

To map cell velocities during wound healing we used particle image velocimetry (PIV) on consecutive image pairs. Resulting maps revealed that throughout the closure process cell velocities pointed uniformly towards the wound and were highest at the leading edge (Fig. 1m–p). To analyse systematically the spatiotemporal evolution of cell velocity maps we computed the average radial velocity as a function of distance from the wound edge and represented this average as spatiotemporal kymographs (Fig. 1q and Supplementary Methods). Kymographs confirmed systematic gradients of radial velocity decaying away from the leading edge. However, the velocity of each cell row around the wound exhibited a non-monotonic time evolution (Fig. 1r) with a maximum at ∼30 min after the onset of wound healing (∼10 min after starting image acquisition). In contrast with the case of expanding monolayers[24], we did not observe a significant delay in the onset of cell motion between adjacent cell rows, suggesting a mechanism for rapid intercellular coordination specific to wound closure.

[1]Institute for Bioengineering of Catalonia, Barcelona 08028, Spain, [2]Institut Jacques Monod (IJM), Université Paris Diderot, and Unité Mixte de Recherche, 7592 CNRS Paris, France, [3]Department of Civil and Environmental Engineering, University of Waterloo, Waterloo, Ontario N2L 3G1, Canada, [4]Mechanobiology Institute (MBI), National University of Singapore, Singapore 117411, Singapore, [5]Institute for Research in Biomedicine (IRB Barcelona), 08028 Barcelona, Spain, [6]Laboratori de Càlcul Numèric, Department of Applied Mathematics III, Universitat Politècnica de Catalunya, 08036 Barcelona, Spain, [7]Institució Catalana de Recerca i Estudis Avançats (ICREA), 08010 Barcelona, Spain, [8]Unitat de Biofísica i Bioenginyeria, Facultat de Medicina, Universitat de Barcelona, and CIBERES, 08036 Barcelona, Spain. †These authors contributed equally to this work.
*e-mail: benoit.ladoux@univ-paris-diderot.fr; xtrepat@ibecbarcelona.eu

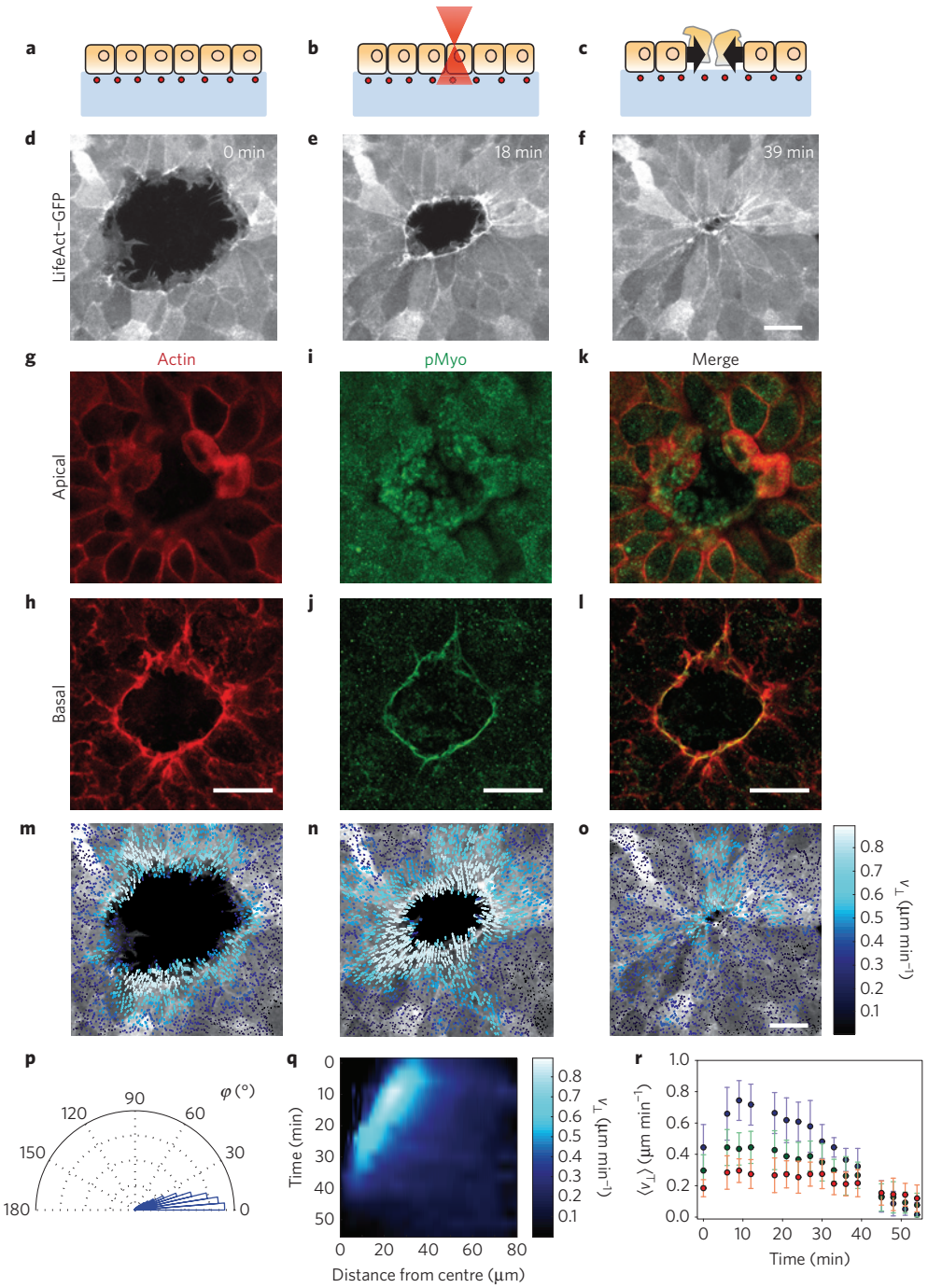

Figure 1 | Cell morphology and kinematics during wound healing. a–c, Scheme of the experimental design. **d–f**, Time course of wound closure in LifeAct-GFP Madin Darby canine kidney cells. Images are maximum projections of confocal *z*-stacks. **g–l**, Staining of phalloidin and pMyo at the apical (**g**,**i**,**k**) and basal (**h**,**j**,**l**) planes. **m–o**, Vectorial representation of cell velocities measured by particle image velocimetry at the same time points as in **d–f**. **p**, Distribution of the angle φ between cell velocities and the direction normal to the wound edge. Data are a pool of all time points for one experiment. **q**, Kymograph of the radial component of cell velocities (Supplementary Methods). **r**, Time evolution of cell velocities as a function of the distance from the leading edge. The time axis indicates the time after the beginning of image acquisition (~20 min after wounding). Each data set represents the average radial velocity within concentric rings of width 15 μm (blue for cells located between 0 and 15 μm from the leading edge, green for 15–30 μm, red for 30–45 μm). Error bars represent standard deviation. Missing time points in **r** are due to image refocusing. Data for these time points have been interpolated in **q** to help visualization. All scale bars are 20 μm.

To elucidate the mechanisms driving cellular motions we turned to the measurement of cell–substrate traction forces using monolayer traction microscopy[21] (Fig. 2 and Supplementary Movie 2). The orientation of these forces depended on the curvature of the wound edge. To illustrate this observation we colour-coded traction maps on the basis of the sign of their radial component (Fig. 2a–c). Regions of the leading edge exhibiting a convex contour showed pronounced protrusive activity and traction forces pointing away from the wound (Fig. 2a). In contrast, regions exhibiting a concave contour showed little protrusive activity, an accumulation of actin at the leading edge, and traction forces pointing towards the wound (Fig. 2a). As wound closure progressed, the contour of the

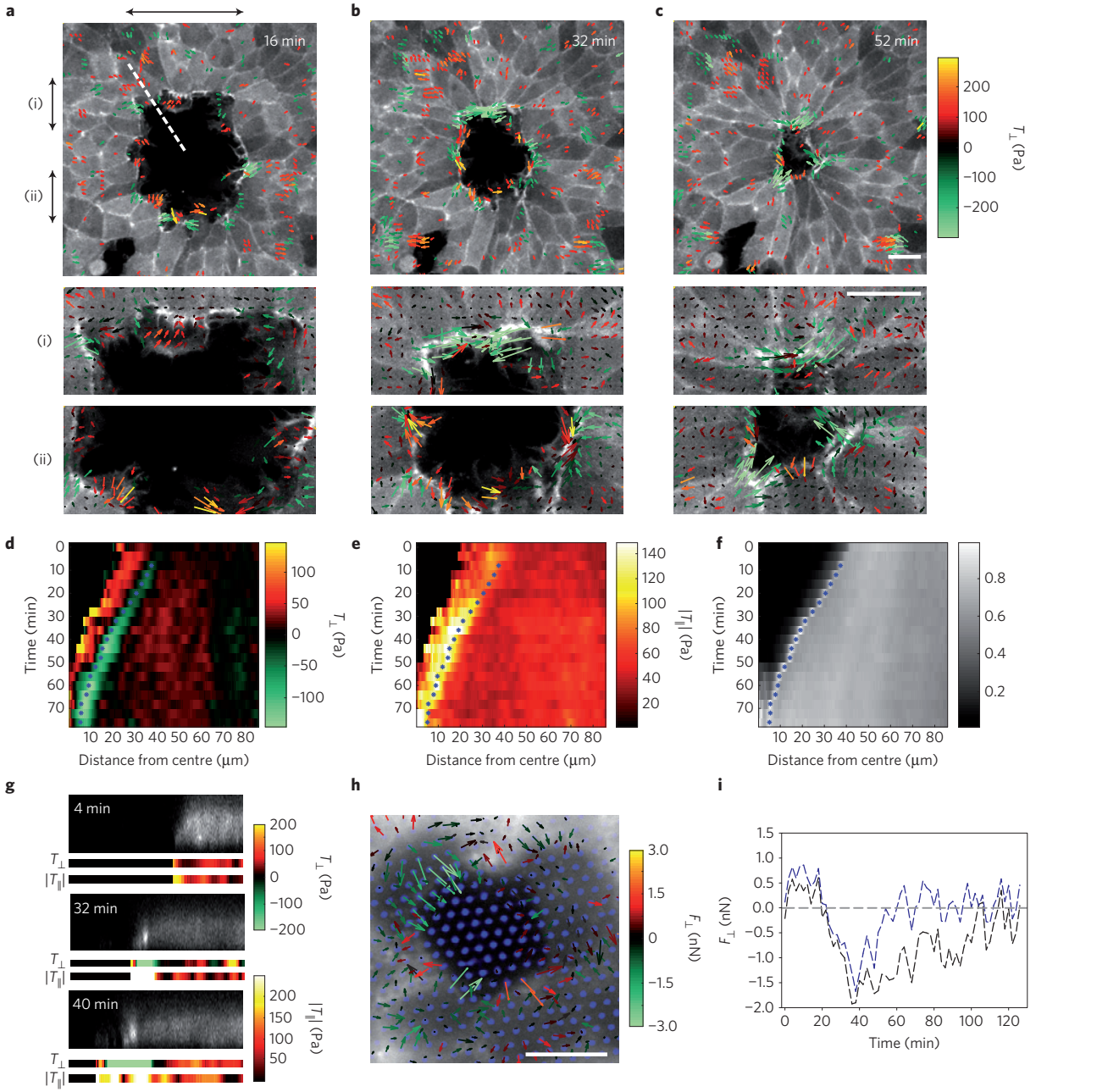

Figure 2 | Traction forces during wound healing. a–c, Vectorial representation of traction forces in LifeAct-GFP Madin Darby canine kidney cells. Colour coding is based on the values of the radial component, with positive forces pointing away from the wound. For clarity, values between −100 and 100 Pa were not plotted. Panels labelled as i and ii show a close-up of the regions indicated by the arrows in **a–c**. Scale bar is 20 μm. **d**, Kymograph for radial traction component $T_\perp$. **e**, Kymograph for tangential traction component $T_\parallel$. **f**, Kymograph of actin-density-based LifeAct-GFP fluorescence. Blue asterisks in **d–f** show the position of the maximum actin density for each time point. **g**, A confocal *z*-section of LifeAct-GFP along the dashed line shown in **a**. Radial and tangential traction forces along that dashed line are shown below LifeAct-GFP images. Total length is 68 μm. **h**, Traction-force maps obtained using micropillar arrays (blue). Scale bar is 10 μm. Forces are colour-coded according to the radial component. **i**, Time evolution of the radial forces of two distinct pillars. Positive forces point towards the wound exterior, whereas negative forces point towards the wound interior.

leading edge became progressively smoother, and tractions pointing towards the wound became ubiquitous (Fig. 2b,c). The radial component of traction forces increased in magnitude with wound curvature and, as closure progressed, this dependence became stronger (Supplementary Fig. 2).

To confirm the results obtained with traction-force microscopy on continuous substrates, we carried out wound-closure experiments in cell monolayers seeded on top of an array of flexible micropillars[19,25–27]. As each micropillar is mechanically uncoupled from its neighbours, traction forces can be computed from a direct measurement of micropillar deflection. Force maps obtained from micropillar deflections confirmed the coexistence of inward- and outward-pointing traction forces at the leading edge of the monolayer (Fig. 2h and Supplementary Movie 3). Given the agreement between traction-force microscopy on continuous substrates and on micropillar arrays, we used the former technique in the remainder of the study.

To isolate systematic force patterns from force fluctuations we computed the average radial ($T_\perp$) and tangential ($T_\parallel$) traction-force components as a function of distance from the wound edge.

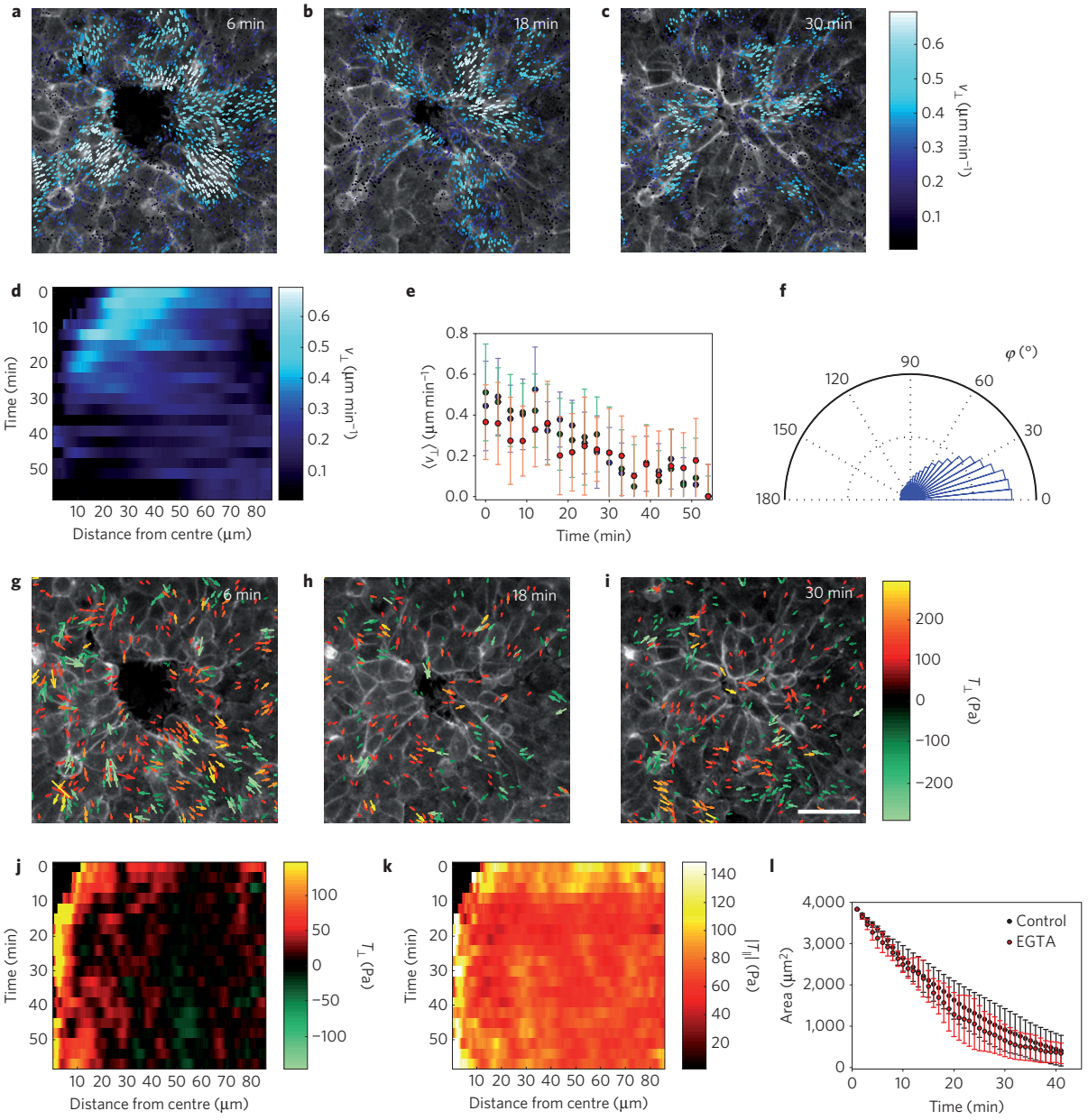

Figure 3 | Traction forces in the absence of an actomyosin ring. a–c, Vectorial plot of velocities measured by particle image velocimetry. **d**, Kymograph of the radial component of velocities. **e**, Time evolution of velocities averaged over adjacent rings of width 15 μm (blue for cells located between 0 and 15 μm from the leading edge, green for 15–30 μm, red for 30–45 μm). Error bars represent standard deviation. **f**, Angular distribution of the angle φ between cell velocities and the direction normal to the wound edge. **g–i**, Vectorial representation of measured tractions. Colour coding is based on the values of the radial component. For clarity, values between −100 and 100 Pa were not plotted. **j**,**k**, Kymographs of radial (**j**) and tangential (**k**) components of traction forces. **l**, Time evolution of the wound area in control cells and EGTA-treated cells. Error bars indicate standard deviation of $n=5$ (control) and $n=6$ (EGTA) samples. All scale bars are 40 μm.

Resulting kymographs showed a remarkable spatiotemporal force pattern (Fig. 2d,e). At the front of the first cell row, the radial force kymograph exhibited a boundary layer of tractions pointing away from the wound up to the end of the closure process. Immediately behind this boundary layer of outward-pointing tractions, but still within the front of the first cell row, there emerged a second layer with a net inward-pointing component increasing in magnitude with time (Fig. 2d). Tractions within this layer were not purely radial, however, and their tangential component was on average larger than the radial one (Fig. 2e). Further away from the leading edge, traction forces were weak but systematically pointing away from the wound, thus showing that crawling forces are not restricted to the first cell row.

A boundary layer of net outward-pointing tractions, which we refer to hereafter as the outward-pointing traction layer (OPTL), has been previously observed in expanding cellular monolayers[19,21]. It has also been reported in monolayers migrating along concave and convex islands on which cells could not adhere[28] and at the leading edge of invading supracellular fingers[27,29,30]. This type of force pattern is typically associated with lamellipodial protrusions[19,21,27,29,30]. In contrast, the observation of a boundary layer of inward-pointing traction forces, which we refer to hereafter as the inward-pointing traction layer (IPTL), is altogether new. The OPTL and the IPTL do not originate solely from averaging two distinct cell populations, one comprising cells favouring protrusions and one comprising cells favouring the actomyosin ring. Instead, outward- and inward-

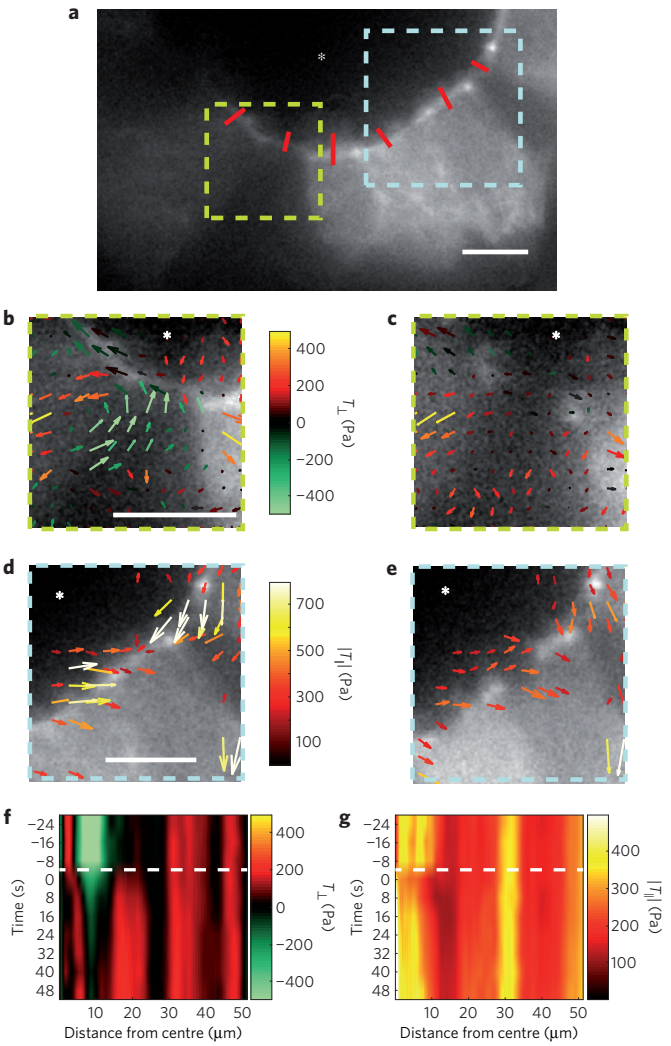

Figure 4 | Traction forces after laser ablation of the actomyosin ring. **a**, Fluorescence image of LifeAct–GFP cells before laser ablation. Red segments mark the sites of ablation. **b**,**c**, A region showing inward-pointing tractions before (**b**) and after (**c**) ring ablation. **c**, Immediately after ablation, normal tractions were abrogated. **d**,**e**, A region with strong tangential tractions before (**d**) and after ablation (**e**). **e**, Tangential tractions were strongly attenuated by ring ablation. For clarity, only forces forming angles of less than 45° with the tangent were plotted. **f**,**g**, Kymograph showing the time evolution of radial (**f**) and tangential (**g**) forces before and after ablation. The cut was performed immediately before $t = 0$ s (dashed white line). All scale bars are 10 μm. Asterisks indicate the interior of the wound.

pointing tractions were seen to coexist at different distances from the leading edge of individual cells (Fig. 2a–c,g). The coexistence of these two distinct force patterns of opposite sign creates a contractile dipole at the tip of protruding leading cells. This dipole was confirmed by monitoring the time evolution of radial forces in micropillar arrays, which showed a clear succession of two phases; in the first phase, cells pulled the pillars towards the monolayer, consistent with the OPTL, whereas in the second phase they pushed them towards the wound, consistent with the IPTL (Fig. 2i). Contractile dipoles between the leading and trailing edges have been extensively reported in single cells migrating in isolation[31–33]. In contrast, the contractile dipoles reported here are restricted to the leading edge of the first cell row. This type of dipole is absent in single cells migrating in isolation[31–33], in cells migrating collectively during monolayer expansion[19,21,26], in invasive supracellular fingers[27,29,30], and in cells enveloping non-adherent islands[28].

The stiffness of the cellular micro-environment has been extensively shown to regulate cell migration and traction forces[34–36]. We next inquired whether patterns of traction forces and wound-healing kinematics were sensitive to the stiffness of the underlying gel. To address this question, we studied wound healing in cell monolayers seeded on 3 kPa substrates (threefold softer than controls). On these soft substrates, cells also assembled a supracellular actomyosin cable, extended multiple protrusions in the wound area, and generated an OPTL at the leading edge and an IPTL immediately behind it (Supplementary Fig. 3a–d). Cells on soft substrates also showed similar sealing times to those on stiff substrates (Supplementary Fig. 3e). This lack of sensitivity of wound-healing forces and kinematics with substrate stiffness is in sharp contrast with the case of single cells migrating in isolation, which showed significantly slower migration velocities on soft substrates (Supplementary Fig. 3f).

A candidate mechanism to explain the IPTL is the transmission of contractile force from the actomyosin ring to the substrate. To study this possibility we first focused on the co-localization of the actomyosin ring and the IPTL. Confocal z-stacks revealed that the actomyosin ring was located basally (Figs 1g–l and 2g) and its assembly coincided in time and space with the emergence of the IPTL. Such co-localization between the ring and the IPTL persisted throughout the closure process (Fig. 2d–f). This evidence strongly suggests that the IPTL originates from the transmission of contractile forces from the basal ring to the underlying substrate.

To further ascertain the origin of the IPTL, we studied the dynamics of wound closure in the absence of a supracellular actomyosin ring. To prevent ring formation, we treated cells with medium containing 4 mM of the calcium chelator EGTA for 1 h before laser ablation and reduced the concentration to 2 mM during the experiment (Fig. 3 and Supplementary Movie 4). Calcium chelation weakened cell–cell junctions behind the leading edge but did not fully disrupt them as shown by the presence of E-cadherin and ZO-1 at intercellular contacts (Supplementary Fig. 1c,d). In contrast, calcium chelation prevented the assembly of a supracellular actomyosin ring at the wound edge (Fig. 3a–c). Under these conditions, the sealing time was similar to control wounds (Fig. 3l) but submarginal cells moved faster (Fig. 3a–e) and exhibited a loss of directionality (Fig. 3f). Importantly, impairment of the actomyosin ring prevented the emergence of the IPTL (Fig. 3j). Instead, average tractions pointed away from the wound, giving rise to an OPTL that spanned multiple cell rows, which indicates a cell-crawling mechanism involving cooperative force transmission in the radial direction as in a tug-of-war[21] (Fig. 3g–k).

Besides preventing formation of the actomyosin ring, calcium chelation mediates other effects that might also contribute to the loss of the IPTL. Thus, to further ascertain that the IPTL is caused by transmission of forces from the ring to the substrate, we ablated the ring at multiple locations and studied the resulting changes in traction forces (Fig. 4a and Supplementary Movie 5). Immediately after ablation, we observed a sudden reduction of inward-pointing traction forces under the ring and behind it (Fig. 4b,c). This reduction became more pronounced with time and, 30 s after ablation, inward-pointing traction forces were abrogated (Fig. 4f). Taken together, our results establish that the IPTL originates from transmission of forces from the ring to the substrate.

Our findings put forward a physical picture in which the OPTL originates from lamellipodial forces, whereas the IPTL originates from transmission of forces from the ring to the substrate. To evaluate whether these force contributions are sufficient to recapitulate the observed wound-closure dynamics we developed a two-dimensional cellular *in silico* model (Supplementary Note 1). To build the model, lamellipodia and gel tractions were added to a finite-element-based γ–μ model of cell mechanics[37,38] (Supplementary Figs 7 and 8). Tensions arising from general cortical

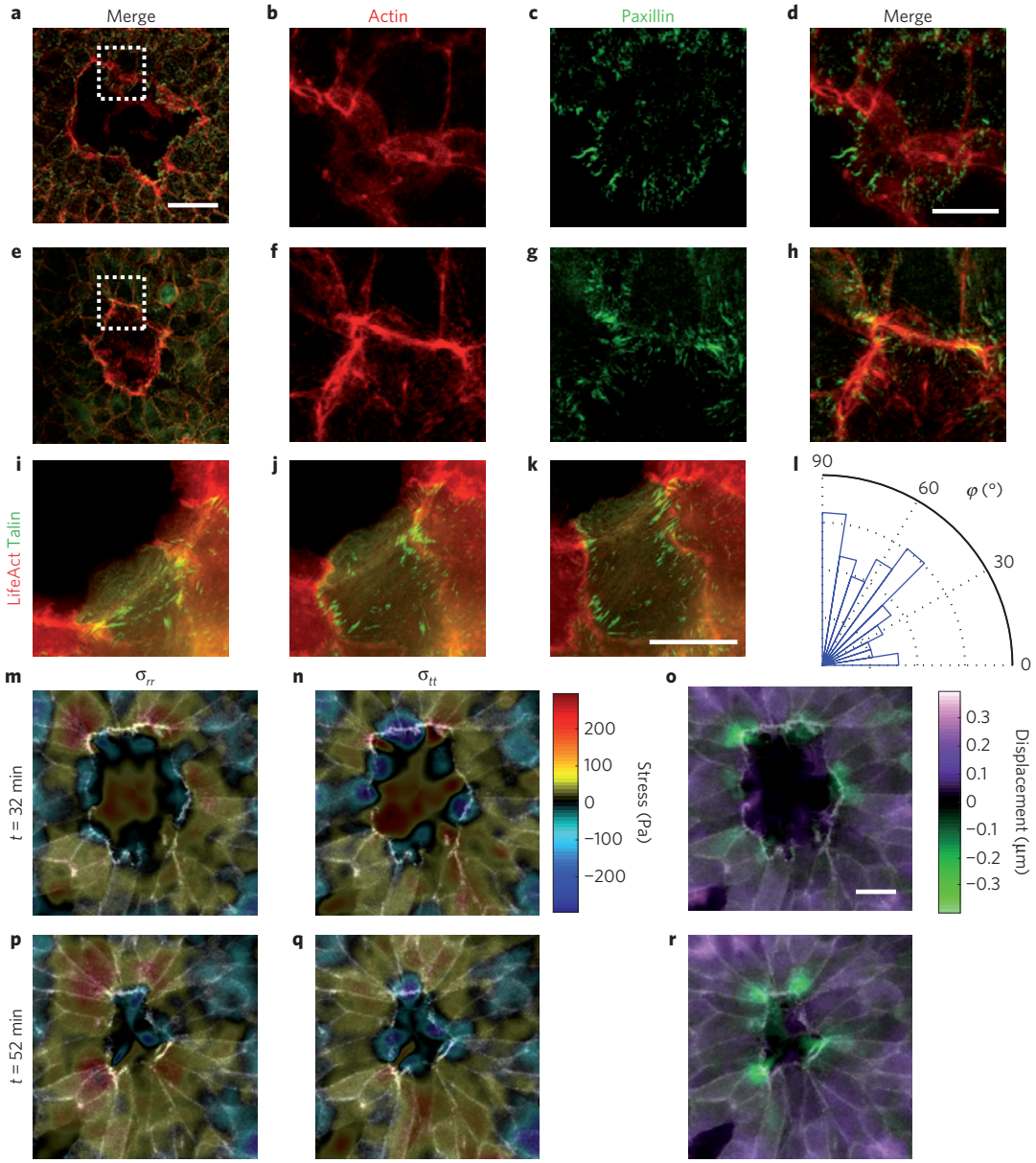

Figure 5 | Force transmission from the ring to the substrate creates heterogeneous stresses and inward-pointing displacements of the underlying substrate. a–h, Representative immunofluorescence micrographs of paxillin and F-actin showing the characteristic structural organization of the leading edge during early (**a–d**) and late (**e–h**) stages of wound closure. **a–d**, During initial stages, focal adhesions were localized at the tip of lamellipodia and were perpendicular to the leading edge. **e–h**, During later stages, focal adhesions appeared under the actomyosin ring. **i–k**, Time-lapse snapshots of Madin Darby canine kidney cells expressing LifeAct-Ruby and talin-GFP at three different time points of wound closure (Supplementary Movie 4). **l**, Angular distribution of focal adhesion orientation with respect to the normal direction (0° is normal to the ring, $n = 112$ focal adhesions from five experiments). The analysis is performed in a 3-μm-thick band located immediately behind the ring (including the ring). **m–r**, Substrate stress and displacements during wound healing. **m**,**p**,**n**,**q**, Radial normal stress (σ_{rr}; **m**,**p**) and tangential normal stress (σ_{tt}; **n**,**q**) in the upper surface of the gel during the latest stages of wound closure. **o**,**r**, Radial displacement of the gel surface. Negative displacements point towards the wound. The two time points considered in **m–r** correspond to **b** and **c** in Fig. 2. Scale bars are 40 μm for **a** and **e**, 10 μm for **b–d** and **f–k**, and 20 μm for **o**.

contraction and actomyosin-ring forces were assumed to act along the cell boundaries while the cytoplasm in the cells was assumed to be viscous and incompressible. Lamellipodia were assumed to arise randomly from any cell edge, but particularly from the edges along the wound perimeter, and to attach to the underlying gel. Viscous drag was assumed to act between the cells and the gel.

Under such assumptions, the model shows that the wound can close either through cell crawling or through purse-string contraction (Supplementary Fig. 9a–d). Lamellipodial protrusions generate an OPTL whereas transmission of tension from the ring to the substrate generates an IPTL. If both mechanisms coexist, the model is able to recapitulate wound-closure kinematics as well as patterns of traction forces in the radial direction (Supplementary Fig. 9e,f). However, the model is unable to explain the striking observation of large traction forces in the tangential direction (Fig. 2b,e). In fact, if the ring had a circular contour and carried constant tension it would produce no tangential traction forces at all. This suggests that an additional mechanism needs to be accounted for to fully explain traction-force generation at the ring.

To address this issue we focused on the structure and localization of focal adhesions. At the leading tip of lamellipodia, staining of paxillin revealed that focal adhesions were perpendicular to the

cell edge (Fig. 5a–d). This geometrical organization is characteristic of lamellipodia-driven cell migration[24,29,30] and is consistent with the force pattern observed at the OPTL. We also observed an accumulation of focal adhesions underneath the actomyosin ring, which is consistent with our conclusion that transmission of force from the ring to the substrate gives rise to the IPTL. Importantly, a large fraction of focal adhesions under the ring was tangential to the wound (Fig. 5e–h,l and Supplementary Fig. 4). We confirmed this observation in wound-closure experiments using LifeAct–Ruby cells expressing talin–GFP (Fig. 5i–k and Supplementary Movie 6). These measurements suggest that the source of high tangential tractions in force kymographs is the transmission of tension from the ring to the substrate at tangential focal adhesions (Fig. 2e). This was confirmed by ablation of the ring, which caused an instantaneous drop in tangential traction forces (Fig. 4d,e,g).

If the ring is transmitting forces to the substrate in the tangential direction, then the tension it carries must be heterogeneous in space. To assess tension heterogeneity in the ring, we computed the two-dimensional stress tensor (σ) at the gel interface with the epithelium. This tensor measures the extent to which traction forces generated by cells produce tension or compression at any given point and direction of the gel surface (Supplementary Methods). To take into account the geometry of the experiments, we focused on the normal components of σ in the directions that are perpendicular (σ_{rr}) and tangential (σ_{tt}) to the actomyosin ring. The resulting stress maps, which are not to be confused with traction maps, showed strong spatial heterogeneities under the actomyosin ring with a sharp alternation between compressive and tensile stresses (Fig. 5m,n,p,q). These spatial heterogeneities are inconsistent with the current understanding of wound-closure mechanisms based on a continuous ring carrying homogeneous tension. Rather, they point to a ring structure that is heterogeneous in space and transmits part of its contractile tension to the substrate through force dipoles oriented tangentially to the wound edge. When this key feature was added to our computational model, kymographs of all force components were successfully reproduced (Supplementary Note 1 and Supplementary Fig. 9g,h).

Exerting traction forces tangentially to the wound would seem counterproductive to drive the cell sheet forward and to extrude damaged cells upwards. Analysis of substrate displacements within the underlying gel leads to a quite different conclusion, however. When a contractile force dipole is applied to the surface of an elastic material with a positive Poisson's ratio, it generates material displacements towards the dipole centre and normally to the dipole's direction. If several such dipoles are arranged in an annular geometry, their contraction will result in a net displacement of the gel surface towards the centre of the ring (Fig. 5o,r, Supplementary Note 2 and Supplementary Fig. 11a). Thus, by applying traction forces tangentially to the wound, cells create net substrate displacements that are radial and point towards the wound, thereby contributing to drag the cell sheet into the wound area (Supplementary Note 2). These displacement patterns are mechanically analogous to those that would result from the active contraction of the tissue underlying the wound, as previously proposed in experimental models of embryonic wound healing[7].

Heterogeneous and anisotropic substrate deformations have been extensively shown to guide cell migration through mechanotransduction processes that remain poorly understood[39–42]. In the case of MDCK cell sheets, for example, self-generated substrate displacements have been shown to precede cellular velocities[40]. Thus, in addition to dragging the cell sheet forward passively, the inward-pointing substrate displacements reported here are also likely to steer cell migration through active mechanotransduction mechanisms. We note that these mechanisms are enhanced on soft substrates, where displacements are higher. As such, they seem reasonable candidates to explain why isolated cells are slower on soft substrates whereas wound-closure rates are paradoxically not (Supplementary Fig. 3e,f).

Our experimental and computational findings establish a new quantitative scenario for the mechanisms driving wound closure in an epithelial sheet. According to this scenario, collective cell crawling is responsible for the initial steps of wound closure but the latest stages of the process involve cooperation between cell crawling and contraction of a supracellular actomyosin ring at the leading edge. Our study reveals that this supracellular ring is a much more versatile structure than previously thought and serves at least two purposes. First, it contributes to wound closure through its well-known purse-string mechanism[2,3,8–10,15]. Second, it transmits part of its contractile force to the substrate through focal adhesions that are mainly tangential to the wound. These contractile forces induce a displacement of the underlying gel towards the wound area and thus tend to steer the monolayer forward. The leading-edge dynamics and force patterns reported here are qualitatively distinct from any previous observation in single or collective cell systems[19,21,26–29,32,33,43,44]. As such, they constitute a starting point in the search for new mechanotransduction strategies in wound closure as well as in the broader context of morphogenesis.

Methods

Traction microscopy. Unless noted otherwise, tractions were measured by Fourier-transform traction microscopy with finite gel thickness as described previously[21]. An interrogation window of 32 × 32 pixels and an overlap of 0.75 were used for the analysis of bead displacements.

Polyacrylamide gel preparation. Polyacrylamide gels were prepared by activating glass-bottom Petri dishes by incubation with Bind Silane dissolved in acetic acid and ethanol (following the proportion 1:1:14) during 10 min. After rinsing with ethanol, dishes were allowed to air dry. Meanwhile, a mixture of 240 µl NHS (10 mg ml^{-1}), 2.5 µl APS (10%), 0.25 µl TEMED, 12 µl 0.2 µm red beads (Fluospheres, Invitrogen), 126.4 µl of HEPES (10 mM), 93.75 µl of acrylamide (40%), and 25 µl of bisacrylamide (2%) was prepared, to obtain gels of 9 kPa in Young's modulus[45]. Twelve microlitres of this mixture was added to a Petri dish, flattened with an 18 mm glass coverslip and allowed to polymerize for 30–45 min. Deionized water was then added to peel off the glass coverslip. Collagen I was added at 0.1 mg ml^{-1} and incubated at 4 °C overnight.

Micropillar arrays. In selected experiments, traction forces were measured using a dense array of fibronectin-coated polydimethylsiloxane micropillars[19,25,27]. Micropillars (3 µm height, 1 µm diameter, 2 µm centre-to-centre distance) arranged in a hexagonal grid were moulded from a silicon master as previously described[19,25,27]. Custom-made multiple-particle tracking software was used to calculate the deflection of the pillars from the undeformed array.

Focal adhesion analysis. Paxillin fluorescent images obtained by immunostaining were segmented by thresholding. Segmented regions were fitted to an ellipse to obtain the eccentricity and orientation. Only adhesions with sizes between 5 and 100 pixels and eccentricity above 0.5 were included in the analysis.

Cell culture. MDCK II cells and stable cell lines expressing LifeAct–GFP or LifeAct–Ruby were cultured with Dulbecco's modified Eagle's medium supplemented with 10% fetal bovine serum, 100 U ml^{-1} of penicillin and 100 µg ml^{-1} of streptomycin. The selection antibiotic geneticin was added at 0.5 mg ml^{-1} for LifeAct stable cell lines. Cells were maintained at 37 °C in a humidified atmosphere with 5% CO_2.

Laser ablation and time-lapse imaging. The set-up used is described in ref. 46. After wounding, time-lapse imaging of the gel surface and of the overlying cells was performed using an inverted Nikon confocal microscope, equipped with an incubator to maintain the samples at 37 °C and 5% CO_2. Laser cutting and traction microscopy were performed in different set-ups. As such there was an average delay of ∼20 min between wounding and the beginning of image acquisition. Image size was 512 × 512 pixels.

Velocity measurements. Velocity maps were obtained by PIV with continuous window shift with an interrogation window of 64 × 64 pixels and overlap of 0.75.

Transfection. To image talin during wound closure we used CellLight talin–GFP. Cells were seeded at low density. When cells were completely attached to the substrate we added 10 µl of the product in 2 ml of medium. Cells were used 16 h after transfection.

Immunofluorescence. Cells were fixed with 4% paraformaldehyde (in PBS) for 15 min at room temperature (in EGTA experiments paraformaldehyde was diluted in a 4 mM EGTA solution). Permeabilization was achieved by incubating with 0.25% Triton X-100 (in PBS) for 20 min at room temperature. Cells were saturated with 1% BSA (in PBS) and incubated during 30 min. In the case of paxillin, 10% FBS (in PBS) was used as the blocking solution and cells were incubated for 60 min. Primary antibodies were added with corresponding blocking solution at 1:1,000 dilution for ZO-1 and E-cadherin and 1:200 for paxillin and phospho-MLC and incubated for 1–2 h. Secondary antibodies were added at 1:200 dilution (with 1:1,000 of phalloidin if needed) and incubated for 1–2 h.

Received 20 September 2013; accepted 20 June 2014; published online 3 August 2014

References

1. Shaw, T. J. & Martin, P. Wound repair at a glance. *J. Cell Sci.* **122,** 3209–3213 (2009).
2. Sonnemann, K. J. & Bement, W. M. Wound repair: Toward understanding and integration of single-cell and multicellular wound responses. *Annu. Rev. Cell Dev. Biol.* **27,** 237–263 (2011).
3. Cordeiro, J. O. V. & Jacinto, A. N. The role of transcription-independent damage signals in the initiation of epithelial wound healing. *Nature Rev. Mol. Cell Biol.* **14,** 249–262 (2013).
4. Crosby, L. M. & Waters, C. M. Epithelial repair mechanisms in the lung. *Am. J. Physiol. Lung Cell. Mol. Physiol.* **298,** L715–L731 (2010).
5. Arwert, E. N., Hoste, E. & Watt, F. M. Epithelial stem cells, wound healing and cancer. *Nature Rev. Cancer* **12,** 170–180 (2012).
6. Kuipers, D. *et al.* Epithelial repair is a two-stage process driven first by dying cells and then by their neighbours. *J. Cell Sci.* **127,** 1229–1241 (2014).
7. Davidson, L. A., Ezin, A. M. & Keller, R. Embryonic wound healing by apical contraction and ingression in *Xenopus laevis*. *Cell Motil. Cytoskeleton* **53,** 163–176 (2002).
8. Anon, E. *et al.* Cell crawling mediates collective cell migration to close undamaged epithelial gaps. *Proc. Natl Acad. Sci. USA* **109,** 10891–10896 (2012).
9. Klarlund, J. K. Dual modes of motility at the leading edge of migrating epithelial cell sheets. *Proc. Natl Acad. Sci. USA* **109,** 15799–15804 (2012).
10. Tamada, M., Perez, T. D., Nelson, W. J. & Sheetz, M. P. Two distinct modes of myosin assembly and dynamics during epithelial wound closure. *J. Cell Biol.* **176,** 27–33 (2007).
11. Abreu-Blanco, M. T., Verboon, J. M., Liu, R., Watts, J. J. & Parkhurst, S. M. Drosophila embryos close epithelial wounds using a combination of cellular protrusions and an actomyosin purse string. *J. Cell Sci.* **125,** 5984–5997 (2012).
12. Martin, P. & Lewis, J. Actin cables and epidermal movement in embryonic wound healing. *Nature* **360,** 179–183 (1992).
13. Bement, W. M., Forscher, P. & Mooseker, M. S. A novel cytoskeletal structure involved in purse string wound closure and cell polarity maintenance. *J. Cell Biol.* **121,** 565–578 (1993).
14. Jacinto, A., Woolner, S. & Martin, P. Dynamic analysis of dorsal closure in Drosophila: From genetics to cell biology. *Dev. Cell* **3,** 9–19 (2002).
15. Hutson, M. S. *et al.* Forces for morphogenesis investigated with laser microsurgery and quantitative modeling. *Science* **300,** 145–149 (2003).
16. Antunes, M., Pereira, T., Cordeiro, J. V., Almeida, L. & Jacinto, A. Coordinated waves of actomyosin flow and apical cell constriction immediately after wounding. *J. Cell Biol.* **202,** 365–379 (2013).
17. Fenteany, G., Janmey, P. A. & Stossel, T. P. Signaling pathways and cell mechanics involved in wound closure by epithelial cell sheets. *Curr. Biol.* **10,** 831–838 (2000).
18. Omelchenko, T., Vasiliev, J. M., Gelfand, I. M., Feder, H. H. & Bonder, E. M. Rho-dependent formation of epithelial 'leader' cells during wound healing. *Proc. Natl Acad. Sci. USA* **100,** 10788–10793 (2003).
19. Roure, O. D. *et al.* Force mapping in epithelial cell migration. *Proc. Natl Acad. Sci. USA* **102,** 2390–2395 (2005).
20. Poujade, M. *et al.* Collective migration of an epithelial monolayer in response to a model wound. *Proc. Natl Acad. Sci. USA* **104,** 15988–15993 (2007).
21. Trepat, X. *et al.* Physical forces during collective cell migration. *Nature Phys.* **5,** 426–430 (2009).
22. Meghana, C. *et al.* Integrin adhesion drives the emergent polarization of active cytoskeletal stresses to pattern cell delamination. *Proc. Natl Acad. Sci. USA* **108,** 9107–9112 (2011).
23. Cochet-Escartin, O., Ranft, J., Silberzan, P. & Marcq, P. Border forces and friction control epithelial closure dynamics. *Biophys. J.* **106,** 65–73 (2014).
24. Serra-Picamal, X. *et al.* Mechanical waves during tissue expansion. *Nature Phys.* **8,** 628–634 (2012).
25. Tan, J. L. *et al.* Cells lying on a bed of microneedles: An approach to isolate mechanical force. *Proc. Natl Acad. Sci. USA* **100,** 1484–1489 (2003).
26. Saez, A. *et al.* Traction forces exerted by epithelial cell sheets. *J. Phys. Condens. Matter* **22,** 194199 (2010).
27. Reffay, M. *et al.* Interplay of RhoA and mechanical forces in collective cell migration driven by leader cells. *Nature Cell Biol.* **16,** 217–223 (2014).
28. Kim, J. H. *et al.* Propulsion and navigation within the advancing monolayer sheet. *Nature Mater.* **12,** 856–863 (2013).
29. Vedula, S. R. K. *et al.* Emerging modes of collective cell migration induced by geometrical constraints. *Proc. Natl Acad. Sci. USA* **109,** 12974–12979 (2012).
30. Vedula, S. R. K. *et al.* Epithelial bridges maintain tissue integrity during collective cell migration. *Nature Mater.* **13,** 87–96 (2013).
31. Dembo, M. & Wang, Y. L. Stresses at the cell-to-substrate interface during locomotion of fibroblasts. *Biophys. J.* **76,** 2307–2316 (1999).
32. Wang, N. *et al.* Cell prestress I stiffness and prestress are closely associated in adherent contractile cells. *Am. J. Physiol. Cell Physiol.* **282,** C606–C616 (2002).
33. Bastounis, E. *et al.* Both contractile axial and lateral traction force dynamics drive amoeboid cell motility. *J. Cell Biol.* **204,** 1045–1061 (2014).
34. Lo, C. M., Wang, H. B., Dembo, M. & Wang, Y. L. Cell movement is guided by the rigidity of the substrate. *Biophys. J.* **79,** 144–152 (2000).
35. Saez, A., Ghibaudo, M., Buguin, A., Silberzan, P. & Ladoux, B. Rigidity-driven growth and migration of epithelial cells on microstructured anisotropic substrates. *Proc. Natl Acad. Sci. USA* **104,** 8281–8286 (2007).
36. Ng, M. R., Besser, A., Danuser, G. & Brugge, J. S. Substrate stiffness regulates cadherin-dependent collective migration through myosin-II contractility. *J. Cell Biol.* **199,** 545–563 (2012).
37. Chen, H. H. & Brodland, G. W. Cell-level finite element studies of viscous cells in planar aggregates. *J. Biomech. Eng.* **122,** 394–401 (2000).
38. Brodland, G. W., Viens, D. & Veldhuis, J. H. A new cell-based FE model for the mechanics of embryonic epithelia. *Comput. Methods Biomech. Biomed. Eng.* **10,** 121–128 (2007).
39. Reinhart-King, C. A., Dembo, M. & Hammer, D. A. Cell–cell mechanical communication through compliant substrates. *Biophys. J.* **95,** 6044–6051 (2008).
40. Angelini, T. E., Hannezo, E., Trepat, X., Fredberg, J. J. & Weitz, D. A. Cell migration driven by cooperative substrate deformation patterns. *Phys. Rev. Lett.* **104,** 168104 (2010).
41. Plotnikov, S. V., Pasapera, A. M., Sabass, B. & Waterman, C. M. Force fluctuations within focal adhesions mediate ECM-rigidity sensing to guide directed cell migration. *Cell* **151,** 1513–1527 (2012).
42. Roca-Cusachs, P., Sunyer, R. & Trepat, X. Mechanical guidance of cell migration: Lessons from chemotaxis. *Curr. Opin. Cell Biol.* **25,** 543–549 (2013).
43. Behrndt, M. *et al.* Forces driving epithelial spreading in zebrafish gastrulation. *Science* **338,** 257–260 (2012).
44. Fernandez-Gonzalez, R. & Zallen, J. A. Wounded cells drive rapid epidermal repair in the early Drosophila embryo. *Mol. Biol. Cell* **24,** 3227–3237 (2013).
45. Yeung, T. *et al.* Effects of substrate stiffness on cell morphology, cytoskeletal structure, and adhesion. *Cell Motil. Cytoskeleton* **60,** 24–34 (2005).
46. Colombelli, J., Grill, S. W. & Stelzer, E. H. K. Ultraviolet diffraction limited nanosurgery of live biological tissues. *Rev. Sci. Instrum.* **75,** 472–478 (2004).

Acknowledgements

We thank M. Bintanel and F. Margadant for technical assistance and P. Roca-Cusachs and members of the Trepat laboratory for discussions. This research was supported by Fondation pour la Recherche Médicale (E.A.), the Spanish Ministry for Economy and Competitiveness (BFU2012-38146 to X.T., Juan de la Cierva Fellowship JCI-2012-15123 to V.C.), the European Research Council (Grant Agreement 242993, X.T.), the Agence Nationale de la Recherche (ANR 2010 BLAN 1515, B.L.), the Institut Universitaire de France (B.L.), the Human Frontier Science Program (grant RGP0040/2012, B.L.), the Mechanobiology Institute of Singapore (B.L.), and the Natural Sciences and Engineering Research Council of Canada (NSERC, J.H.V. and G.W.B.).

Author contributions

A.B., E.A., J.C., B.L. and X.T. designed experiments; A.B. and E.A. performed experiments; A.B. analysed experimental data; A.B., V.C. and J.J.M. developed computational tools for data and stress analysis; M.G. analysed micropillar data; J.C. contributed technology; V.C., J.H.V. and G.W.B. built computational models and performed simulations; A.B., E.A., V.C., J.J.M., G.W.B., B.L. and X.T. wrote the manuscript; all authors discussed and interpreted results and commented on the manuscript; B.L. and X.T. conceived and supervised the project.

Additional information

Supplementary information is available in the online version of the paper. Reprints and permissions information is available online at www.nature.com/reprints. Correspondence and requests for materials should be addressed to B.L. or X.T.

Competing financial interests

The authors declare no competing financial interests.